

## OPTICS

# Exchange coupling–mediated broken symmetries in Ta<sub>2</sub>NiSe<sub>5</sub> revealed from quadrupolar circular photogalvanic effect

Harshvardhan Jog<sup>1</sup>, Luminita Harnagea<sup>2</sup>, Eugene J. Mele<sup>3</sup>, Ritesh Agarwal<sup>1\*</sup>

In low–electron density materials, interactions can lead to highly correlated quantum states of matter. Ta<sub>2</sub>NiSe<sub>5</sub>, an excitonic insulator (EI) candidate, exists in a novel broken-symmetry phase below 327 K, characterized by robust exchange interaction and electron–lattice coupling. We study this phase of Ta<sub>2</sub>NiSe<sub>5</sub> using the quadrupole circular photogalvanic effect (QCPGE). Light–matter interaction in Ta<sub>2</sub>NiSe<sub>5</sub> mediated by electric quadrupole/magnetic dipole coupling produces helicity–dependent DC response even with centrosymmetry, making it particularly sensitive to certain other broken symmetries. We show that the exchange interaction in Ta<sub>2</sub>NiSe<sub>5</sub> can lead to a triclinic structure with a broken C<sub>2</sub> symmetry. Our results provide an incisive probe of the symmetries of the low-temperature phase of Ta<sub>2</sub>NiSe<sub>5</sub> and add new symmetry constraints to the identification of a strongly correlated EI phase. The high sensitivity of QCPGE to subtle symmetry breaking in centrosymmetric systems will enable its use in studying other complex crystalline systems.

## INTRODUCTION

Symmetry breaking in condensed matter plays a fundamental role in the classification of phases of matter and ultimately in understanding their properties (1–5). Precisely defining the symmetries and broken symmetries in a system is therefore critically important, particularly in complex materials where various degrees of freedom can be coupled in the presence of strong correlation effects (6–11). Excitonic insulators (EIs) form a class of interacting many-body states where electrons and holes spontaneously condense into an insulating state because of the development of a coherent state of correlated electron-hole pairs (12–14). Such a many-body state can occur in low–electron density materials with a small bandgap or with a small band overlap, and in both cases, a many-body gap opens up as the system transitions into the EI phase (15). Candidate materials have been proposed to host EI phases, including Tm(Se,Te) (13, 16), 1T-TiSe<sub>2</sub> (17, 18), and Ta<sub>2</sub>NiSe<sub>5</sub> (19, 20). However, in all the proposed material systems, a substantial coupling of the collective electronic degrees of freedom to the lattice requires an accompanying structural distortion when the system enters the EI phase, which complicates efforts to systematically study the phenomena. For example, in Tm(Se,Te) and 1T-TiSe<sub>2</sub>, an indirect band alignment in the material forces the structural transition at nonzero **q** as the material condenses into the excitonic ground state, producing correlated phases such as charge density waves, making it difficult to probe the pure EI phase (21, 22). On the other hand, in Ta<sub>2</sub>NiSe<sub>5</sub>, the instability occurs at **q** = 0, and although it is also accompanied by a structural change, it does not form a charge density wave phase (23). A recent paper claims strong evidence that Ta<sub>2</sub>NiSe<sub>5</sub> hosts such an EI phase in the low-temperature regime (24). However, characterizing the symmetries in Ta<sub>2</sub>NiSe<sub>5</sub> in its different phases

and its effect on the electronic correlations still remains an important problem to elucidate the interplay of a variety of electronic and structural effects on the possible formation of this EI phase (25, 26).

Here, we report the observation of a new variant of the second-order nonlinear circular photogalvanic effect (CPGE), which we call the quadrupolar CPGE (QCPGE), and using it, we deduce that Ta<sub>2</sub>NiSe<sub>5</sub> upon structural transition at 327 K relaxes into a triclinic phase identified by a broken C<sub>2</sub> symmetry. We show that the QCPGE response enables an electric dipole–forbidden transition in a material with bulk inversion symmetry and produces a signal from electric quadrupole/magnetic dipole transitions, which is uniquely sensitive to these symmetries. We further analyze the effects of electronic exchange interactions in Ta<sub>2</sub>NiSe<sub>5</sub> and show that because of the symmetry of its hybridized low-energy bands, the system undergoes relaxation into a C<sub>2</sub> symmetry–broken phase. We find that the QCPGE response from the broken C<sub>2</sub> symmetry is associated with a unique antiresonant line shape arising from the quadrupolar coupling, which is seen experimentally and provides a compelling illustration of the underlying physics.

The crystal structure of Ta<sub>2</sub>NiSe<sub>5</sub> is shown in Fig. 1A. Above 327 K, Ta<sub>2</sub>NiSe<sub>5</sub> has an orthorhombic structure and belongs to the space group *Cmcm* with mirror symmetries normal to all three crystal axes preserved (20). Below the transition temperature at  $T_c = 327$  K, the space group of Ta<sub>2</sub>NiSe<sub>5</sub> has been proposed to be *C2/c*, and it is a quasi–one-dimensional (1D) material with Ni chains surrounded by TaSe<sub>6</sub> tetrahedra on either side of the chains (23). During the second-order phase transition at  $T_c$ , a possible excitonic instability coupled with the freezing of the  $B_{2g}$  phonon modes (23, 27) leads to two effects due to strong electron-phonon coupling in the system (23, 28). First, hybridization of one of the Ta-derived conduction band branches with the Ni-derived valence band takes place, which is absent in the high-temperature phase because of opposite mirror parities with respect to the mirror plane perpendicular to the Ni chains (25, 26). Second, Ta atoms are displaced on either side of the Ni chain antiparallel to the chain direction, which leads to formation of atomic displacements in opposite directions on either side of the Ni chain, breaking the in-plane mirror symmetries (23, 25). The

Copyright © 2022  
The Authors, some  
rights reserved;  
exclusive licensee  
American Association  
for the Advancement  
of Science. No claim to  
original U.S. Government  
Works. Distributed  
under a Creative  
Commons Attribution  
NonCommercial  
License 4.0 (CC BY-NC).

<sup>1</sup>Department of Materials Science and Engineering, University of Pennsylvania, Philadelphia, PA 19104, USA. <sup>2</sup>Department of Physics, Indian Institute of Science Education and Research, Pune, Maharashtra 411008, India. <sup>3</sup>Department of Physics and Astronomy, University of Pennsylvania, Philadelphia, PA 19104, USA.

\*Corresponding author. Email: riteshag@seas.upenn.edu

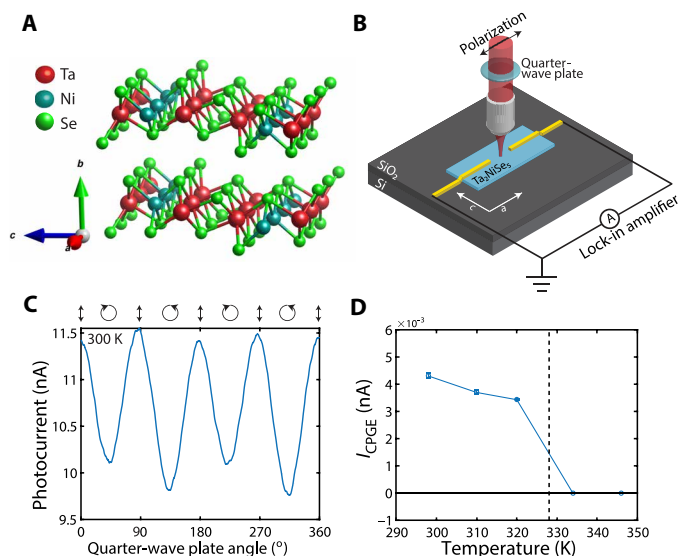


**Fig. 1. Polarization-dependent photocurrent response of  $\text{Ta}_2\text{NiSe}_5$  above and below the transition temperature.** (A) High-temperature crystal structure of  $\text{Ta}_2\text{NiSe}_5$ . The material is quasi-1D in nature with Ni chains along the  $a$  axis surrounded by  $\text{TaSe}_6$  tetrahedra. In the low-temperature phase (below 327 K), the Ta atoms move antiparallel to the Ni chains, thereby breaking all mirror symmetries in the  $a$ - $c$  plane. (B) Schematic of the CPGE experiment setup. The excitation laser was incident along the  $\hat{z}$  direction. See Materials and Methods for details. (C) Polarization-dependent photocurrent at room temperature. A measurable difference between the current corresponding to left and right circularly polarized light was observed indicating the presence of CPGE. (D) Temperature-dependent CPGE photocurrent ( $I_{\text{CPGE}}$ ) shows the disappearance of CPGE above  $T_c = 327$  K as  $\text{Ta}_2\text{NiSe}_5$  goes to the orthorhombic phase. The error bars were obtained by calculating the SD from the fitted CPGE curves using Eq. 1.

distortion also gives rise to a nonzero ferrorotational order,  $\vec{r} \times \vec{P}$ , where  $\vec{r}$  and  $\vec{P}$  denote the position and polarization of the Ta dipoles, respectively (23). The hybridization of the bands and this structural transition are closely related with each other (25).

In the high-temperature phase, the top of the valence band consists mainly of Ni  $3d_{xz}$  and  $3d_{yz}$  orbitals (with some contribution from the Se 4p orbital), while the bottom of the conduction band has largest contribution from the Ta  $5d_{xy}$  orbital and is split into bonding and antibonding states due to opposite parity with respect to the mirror plane parallel to the Ni chains (20, 26). Recent reports (25) have suggested that the transition to low-temperature phase can be characterized by an order parameter measuring the coherence of the Ta and Ni orbitals:  $\Delta_{ij} = \langle c_i^\dagger c_j \rangle$ , where  $c_i^\dagger$  ( $c_j$ ) corresponds to an electron creation (annihilation) operator at  $i = \text{Ta}$  and  $j = \text{Ni}$  sites, which effectively defines the strength of the hybridization of these low-lying states. The order parameter is zero for the high-temperature phase and nonzero for the low-temperature phase. In previous analyses (25), the symmetry of this order parameter was constrained to respect all symmetries of the monoclinic phase. However, first-principles calculations have suggested that the system actually relaxes into a triclinic phase but with small distortions that are not easily identified with conventional experimental techniques (25, 29). A small triclinic distortion may not be picked up using x-ray diffraction but can have consequences for other properties of the system controlled by the crystal symmetries. We find that QCPGE is

sensitive to this symmetry-breaking distortion and can be used to interrogate it in this system.

To carefully investigate the structural symmetries and their relation to the electronic properties of the system, we use CPGE measurements as a spectroscopic probe. In CPGE, the polarity and magnitude of photocurrents can be controlled by the chirality of optical excitation, making it highly sensitive to the local symmetry of the crystal interacting with the incoming light beam (30–33). CPGE can originate from an unequal population of photoexcited carriers in a preferential momentum direction when excited by light with left or right circular polarization. Second harmonic generation is another technique that relies on the local symmetry and electronic properties (34, 35); however, it requires large intensity of incoming light, and  $\text{Ta}_2\text{NiSe}_5$  owing to its small bandgap and large absorption in the visible/near-infrared region of the spectrum suffers photo-damage even at very low powers. In the lowest order, i.e., under the electric dipole approximation, CPGE is only allowed in systems with broken inversion symmetry and then only in the gyrotropic point groups ( $C_1, C_2, C_3, C_4, C_6, C_s, C_{2v}, C_{3v}, C_{4v}, C_{6v}, D_2, D_4, D_{2d}, D_3, D_6, S_4, T$ , and  $O$ ) (36). Studies of CPGE measurements showing responses disallowed in the dipole limit but allowed through terms of higher multipole coupling until now have relied upon materials with broken inversion symmetry while extracting the response terms beyond the lowest order (32, 37). To the best of our knowledge, coupling of higher-order multipoles in CPGE responses in systems that preserve inversion symmetry has not been observed unless the inversion symmetry was explicitly broken by an applied external bias voltage or strain (31, 38). However, we show below that a CPGE response to the electric quadrupole (or magnetic dipole) order can be observed in an inversion-symmetric system and is particularly sensitive to the structural symmetries of the system even with slight distortions associated with symmetry-breaking effects.

## RESULTS

To study the photogalvanic response of  $\text{Ta}_2\text{NiSe}_5$ , we fabricated the electrode geometry shown in Fig. 1B (for material synthesis and fabrication details, see Materials and Methods and figs. S1 and S2). Because the crystal preferentially cleaves such that the length of the crystal along the  $a$  axis is longer than along the  $c$  axis, the crystal orientation can be easily determined to fabricate electrodes in particular directions. Gaussian laser beam profile of a tunable super-continuum laser was used as an excitation source with the wavelength range from 400 to 800 nm. The light was incident normally along the  $-\hat{z}$  direction (Fig. 1B), which corresponds to the  $b$  axis in the crystal geometry. This ensures the elimination of an anisotropic in-plane light momentum, leading to effects such as photon drag effect (30, 39). The light beam (typical power,  $\sim 0.25$  mW) was focused to a spot size of  $\sim 2$   $\mu\text{m}$  at the center of the electrodes (electrode separation was kept  $\sim 15$  to  $20$   $\mu\text{m}$ ) to avoid Schottky field-dependent CPGE from the electrodes (see Materials and Methods) (31).

Polarization-dependent photocurrent measurements were performed under no applied bias using a quarter-wave plate (QWP) to change the helicity of the incident light on the sample. The photocurrent was fitted to the phenomenological equation of photogalvanic effect as given by (30)

$$I(\theta) = I_{\text{CPGE}} \sin(2\theta) + I_{\text{LPGE}} \sin(4\theta + \delta) + I_0 \quad (1)$$

where  $\theta$  is the angle of the fast axis of the QWP with respect to the incoming linear polarization of the laser,  $I_{\text{CPGE}}$  and  $I_{\text{LPGE}}$  are the circular and linear polarization components of the photogalvanic effect, respectively,  $\delta$  is a phase shift in the  $I_{\text{LPGE}}$  component, and  $I_0$  is the polarization-independent background current, which arises because of thermal currents and other extraneous effects. We first measured room-temperature polarization-dependent photocurrent at an excitation wavelength of 725 nm to map the response of the system to changing helicity of the incident light. Notably, we observed a difference in the photocurrent values at  $\theta = 45^\circ$  (left circularly polarized light) and  $\theta = 135^\circ$  (right circularly polarized light), which implies that there is a light helicity-dependent CPGE response from the device (Fig. 1C), although  $\text{Ta}_2\text{NiSe}_5$  does not belong to the gyrotropic group. Furthermore, we observed no CPGE response in  $\text{Ta}_2\text{NiS}_5$  under similar conditions, which is a closely related material with orthorhombic structure at room temperature (40).

The observation of nonzero  $I_{\text{CPGE}}$  is intriguing, because it is doubly forbidden owing to the presence of inversion symmetry and the presence of a  $C_2$  rotation axis along the  $\hat{z}$  direction (incident light direction), in the  $C_{2h}$  point group in the low-temperature phase of  $\text{Ta}_2\text{NiSe}_5$ . Moreover, the CPGE disappeared as we heated the system above the transition temperature into the orthorhombic phase (Fig. 1D and see fig. S3), and thus, its existence is unique to the low-temperature phase. Such symmetry-forbidden nonzero  $I_{\text{CPGE}}$  in the low-temperature phase of  $\text{Ta}_2\text{NiSe}_5$  is of anomalous origin and requires further inspection.

To ensure that the observed effect is an inherently material-dependent effect and does not depend on external factors such as electrode geometry or certain defects, we performed a series of experiments to rule them out. Intensity-dependent measurements showed a linear dependence of  $I_{\text{CPGE}}$  on input power (Fig. 2A) (30–32, 39). To test whether electrode design or their orientation with respect to the crystal axis has any influence on the observed CPGE behavior, we changed the device geometry (Fig. 2B, inset), wherein the electrodes were fabricated aligned along the  $c$  axis (see fig. S4 for an optical image of the device). These devices also clearly showed CPGE under zero bias, indicating that the device geometry has no notable effect on the observed phenomenon. Scanning the laser spot from one end of the electrodes to the other along the  $c$  axis also did not produce any significant change in the CPGE

response (Fig. 2B). Therefore, we conclude that defects, which can also have a nonuniform distribution throughout the material, do not affect the observed response of the system. Other extraneous effects related to strain, exfoliation, or device fabrication are also unlikely to result in these observations because the current will not follow any systematic dependence and will change from different regions of the sample or from sample to sample on the basis of local symmetry breaking. We also performed laser spot size-dependent measurements (Fig. 2C) to rule out any spatially dispersive CPGE (s-CPGE) (32) contributions, which can arise because of nonuniform excitation profile, thereby breaking symmetries in the system that would otherwise disallow CPGE. However, the value of  $I_{\text{CPGE}}$  remained constant as the laser spot diameter was increased. s-CPGE, if present, depends strongly on the laser spot size (optical field gradients) and decreases rapidly as spot size is increased. Therefore, along with no obvious spatial position-dependent CPGE response, we can rule out s-CPGE as a possible candidate for the observed effect. These observations demonstrate that the observation of CPGE under a normally incident laser beam in  $\text{Ta}_2\text{NiSe}_5$  is an intrinsic effect and therefore warrants further examination.

To further understand the observed CPGE response from the low-temperature phase of  $\text{Ta}_2\text{NiSe}_5$ , we performed excitation wavelength-dependent study from which line shapes of resonances can be extracted (Fig. 3A). For device 1 (blue circles), the CPGE shows a clear sign reversal at  $\sim 650$ -nm excitation wavelength along with an antiresonance line shape. Furthermore, for every device that produced the line shape as obtained for device 1, a corresponding device with a flipped version of the response was found with a mirrored behavior (red circles, device 2) along the  $I_{\text{CPGE}} = 0$  axis (also see fig. S4). Such systematic sign reversal in all observed devices points toward an intrinsic origin of the effect. The presence of nonzero CPGE, antiresonance line shape, and mirrored behavior from devices are rather unconventional and need detailed analyses to extract the microscopic physics of the system. Note that device-to-device fabrication variability can lead to differences in the measured magnitude of the CPGE signals; however, the antiresonant line shape is a common feature among all observed devices.

A bulk CPGE response is symmetry forbidden in the low-temperature phase of  $\text{Ta}_2\text{NiSe}_5$  because of the presence of inversion and  $C_{2z}$  rotational symmetry. Therefore, to explain these observations, we considered the following possibilities: (i) electric dipole-induced

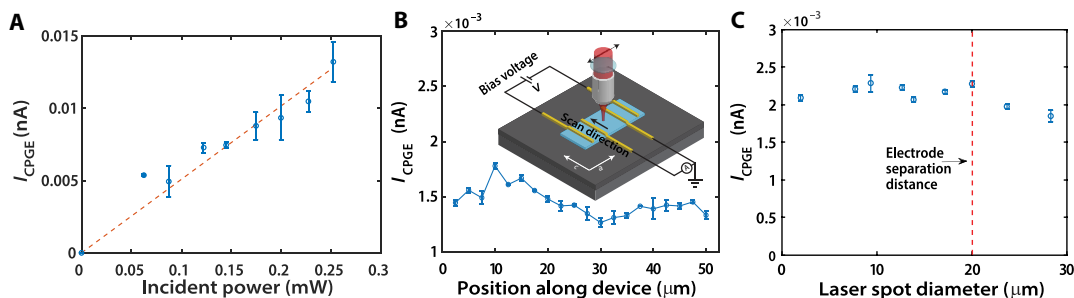


**Fig. 2. Detailed characterization of CPGE signal obtained from  $\text{Ta}_2\text{NiSe}_5$  at room temperature to probe the origins of the anomalous behavior.** (A) Input power dependence of the  $I_{\text{CPGE}}$  response showing a linear dependence to laser power. Red dashed line indicates the linear fit to data. (B) Inset: Changed device design includes two sets of electrodes parallel to the  $c$  axis. The two outer electrodes were used to apply a bias voltage, while the two inner electrodes were used to measure the photocurrent of the device using a lock-in amplifier and perform an excitation position scanning measurement. Main: A typical transverse scanning measurement displays no significant variation in the observed CPGE value. (C) Laser spot size-dependent CPGE response shows no variation with spatial beam profile. In (A) to (C), the error bars were obtained using the SD from the fitted CPGE curves using Eq. 1.

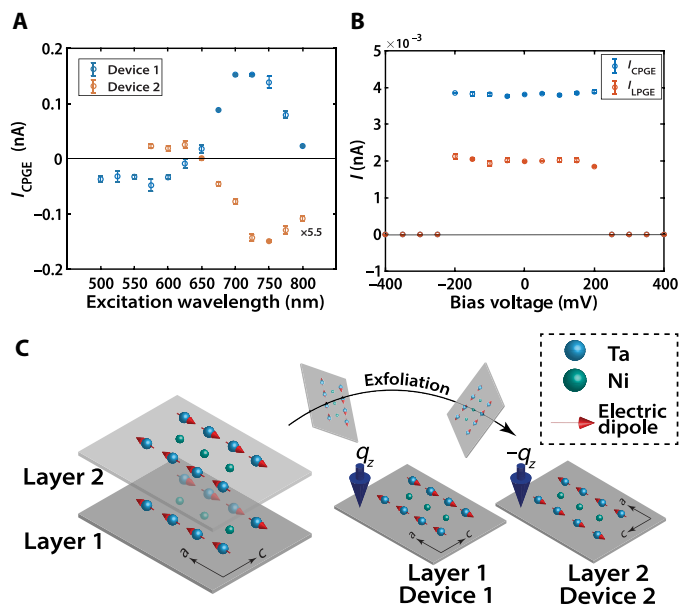


**Fig. 3. Wavelength and bias dependence of CPGE response from  $\text{Ta}_2\text{NiSe}_5$  at room temperature.** (A) Wavelength dependence of the observed CPGE. Two kinds of devices were observed with their behavior mirrored along the  $I_{\text{CPGE}} = 0$  axis. The devices changed the sign of the response at  $\sim 625$ - to  $650$ -nm excitation wavelength, displaying an antiresonant behavior. (B) External bias voltage dependence of the  $I_{\text{CPGE}}$  and the  $I_{\text{LPGE}}$  components of the system. The CPGE and LPGE components displayed a constant value up to  $\pm 200$  mV, after which there was a sudden disappearance of PGE in the system. In (A) and (B), the error bars were obtained using SD from the fitted CPGE curves using Eq. 1. (C) A schematic showing how, after mechanical cleavage, the top and bottom surfaces of the same crystal being mirror images of one another respond to incoming light differently. Probing the top or bottom surface of the crystal is akin to making the change  $q_z \leftrightarrow -q_z$  in the system, reversing the response of the system, leading to the observation of mirrored response along the  $I_{\text{CPGE}} = 0$  axis.

response from possible polar domain walls in the material (40, 41); (ii) a surface response where broken inversion symmetry can lead to an electric dipole response; or (iii) a bulk material response of the next highest-order coupling to the optical field, i.e., the coupling of one quadrupole (or magnetic dipole) moment and one electric dipole order of the incident light fields.

Domain walls are formed in  $\text{Ta}_2\text{NiSe}_5$  by two possible arrangements of the Ta dipoles, with the domain walls having a finite polarization due to parallel arrangement of dipoles on either side (see fig. S7). In the immediate vicinity of a domain wall, the  $C_2$  symmetry is broken, resulting in a local symmetry of  $C_1$ , which can produce a CPGE signal. However, there are two kinds of polar domain walls that form, which are twins and arranged along the  $a$  axis but with the axis of the Ta dipole polarization pointed either along the  $+a$  axis or the  $-a$  axis. This leads to the CPGE contribution from the domain walls on either side of any domain to be equal and opposite (see section S1). A laser spot size of  $\sim 2$   $\mu\text{m}$  will, on average, excite  $\sim 100$  domains of an average size of  $\sim 20$  nm (41) and an equal number of domain walls, but with equal and opposite contributions to the dipolar CPGE that will cancel, leading to a net zero CPGE. The presence of these equal and opposite polar domain wall orientations restores an average  $C_2$  symmetry, leading to a net zero CPGE, as in-plane CPGE is disallowed in the presence of a perpendicular  $C_2$  axis.

Therefore, any contributions originating from polar domain walls in  $\text{Ta}_2\text{NiSe}_5$  can be neglected.

Bias dependence of the CPGE measurement provides further insight to help rule out a purely electric dipole-driven response (Fig. 3B). We applied a bias voltage along the  $a$  axis, which allows a nonzero DC to flow through the device (under no light). The CPGE response was observed to be nearly constant until  $\pm 200$  mV of applied bias, after which there was a sudden disappearance of any polarization-dependent photocurrent although the polarization-independent photocurrent increased with bias (fig. S8). This is in contrast to electric dipole-induced bias-dependent CPGE, which typically gets modulated proportional to the electric-field strength that aids in symmetry breaking (31, 42). Joule heating of the device beyond the transition temperature  $T_c = 323$  K can be ruled out as the heat required to raise the temperature of a typical device by 30 K is at least two orders of magnitude more than the heat generated by resistive heating at the 200-mV bias (see fig. S10 for dark  $I$ - $V$  data in the relevant bias voltage range) (43). The sudden disappearance of response for an applied bias of  $> 200$  mV is therefore intriguing and will be discussed later. The lack of bias-dependent CPGE in addition to lack of any modulation in the transverse scanning measurement (Fig. 2B) helps further rule out the polar domain wall-dependent electric dipole-driven response. Applying an in-plane voltage bias leads to a flow of current in the system with the injection of carriers that change the population of the states near the Fermi level. The bias at which the signal disappears is comparable to the bandgap of the material ( $\sim 160$  meV) (20, 43). Applying a bias populates the states equally above and below the Fermi energy, and the disappearance of PGE is indicative of the fact that unequal population of the hybridized states is important for generation of the PGE in the system. These low-energy states are coupled to high-energy excitations (27), and the disappearance of PGE shows that the population of these states are responsible for the behavior of the system even in the high-energy optical excitation regime.

## DISCUSSION

The main candidates for explaining the observed CPGE are thus limited to either a surface electric dipole response (broken inversion) or a bulk higher-order response in the presence of inversion symmetry. These two can be distinguished by the wavelength dependence of the response. To theoretically model this behavior, we consider three distinct processes as shown by the Feynman diagrams in Fig. 4 (A to C). The first diagram (Fig. 4A) represents the ordinary electric dipole CPGE present in inversion symmetry-broken systems that fall under the gyrotropic point groups and is not applicable to our system. This can be seen schematically in Fig. 4A where for an inversion-symmetric system, one can assign definite parity to each state  $|l\rangle$ ,  $|k\rangle$ ,  $|j\rangle$  while crossing a dipolar vertex, leading to a change in the parity of the states. Hence, if we start with a definite parity to any of the states, then coming back to the same state after two dipolar couplings leads to the opposite parity of the initial state, which sets the amplitude of the process to zero. The second diagram (Fig. 4B) is a previously unidentified bulk process in a system with inversion symmetry, but with a higher-order multipole coupling to the light. We term this contribution the QCPGE. Such a process has one dipole and one quadrupole/magnetic dipole order vertex, down-converting the driving fields to produces a DC response. This process is symmetry-allowed if inversion is preserved,

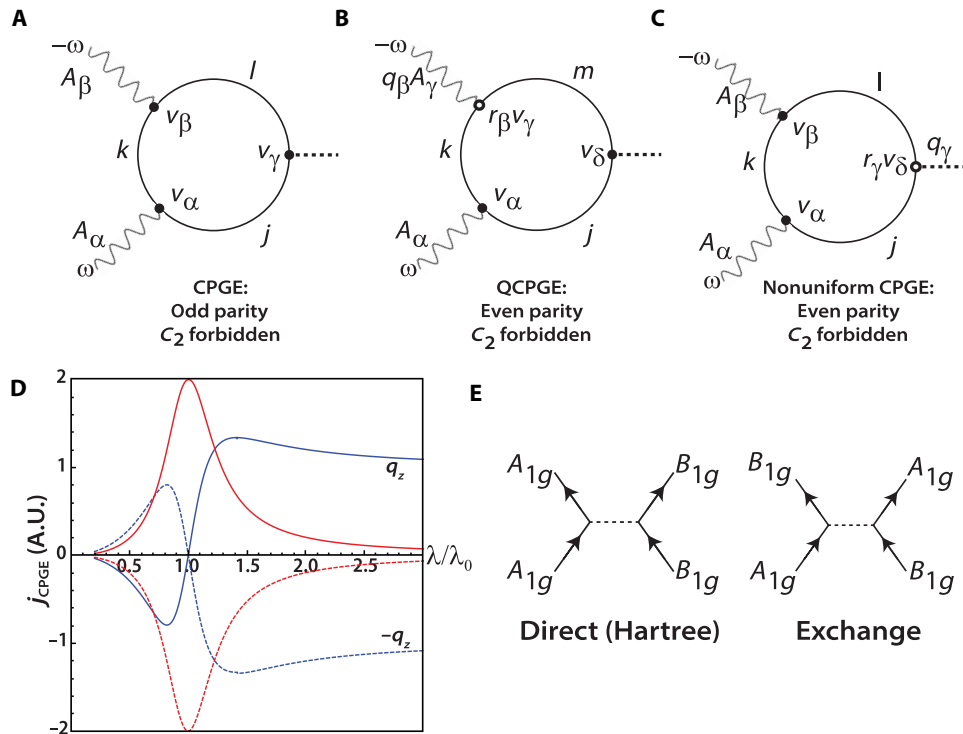


**Fig. 4. Feynman diagrams and associated plots of various processes leading to CPGE in  $\text{Ta}_2\text{NiSe}_5$ .** (A) Ordinary dipole CPGE, which is allowed only in gyrotropic point groups. (B) QCPGE, which is an even-parity response and therefore is allowed in inversion-symmetric materials. However, it is forbidden in systems with an in-plane  $C_2$  rotational symmetry. (C) A nonuniform CPGE response, which is exponentially localized to the surface of the system. Such a response arises because the inversion symmetry is broken at the surface of a material but is forbidden in the presence of an out-of-plane  $C_2$  axis. (D) The wavelength dependence of the processes described in (B) and (C) are shown with blue and red curves, respectively. The blue curve matches well with the experimental response as seen in Fig. 3A in the vicinity of the antiresonance crossing. The model used in the text is simplified and does not consider parameters far away from the resonance/antiresonance region, whereas in the experimental results, these factors may come into play especially at wavelengths much higher or lower than the  $j_{\text{CPGE}} = 0$  crossing point. A.U., arbitrary units. (E) Two possible processes showing interactions between irreducible representations forming the valence and conduction band edges in  $\text{Ta}_2\text{NiSe}_5$ , one representing the direct interaction of bands and the other representing the exchange interaction of the bands. The exchange interactions lead to hybridization of the bands. The expectation value  $\langle \psi_{B_g}^\dagger \psi_{A_g} \rangle$  is non-zero only in the absence of  $C_{2z}$  and  $\sigma_z$  symmetries, because two orbitals with different irreducible representations with respect to these symmetries cannot hybridize.

but it requires the breaking of the  $C_{2z}$  symmetry. This can be easily seen by assigning the irreducible representations  $A$  and  $B$  to the states, and performing a similar symmetry analysis as discussed above, one can see that the system cannot come back to its original state without breaking the  $C_{2z}$  symmetry. The third diagram (Fig. 4C) represents a surface electric dipole response, where the output current is exponentially localized to the surface. Therefore, this process requires that the output current be dependent on the wave vector  $q_z$  in the direction of the incoming photon momentum, and hence, the output current is of a quadrupole/magnetic dipole order. Such a process can be regarded as a variation of the dipole-mediated CPGE diagram but instead with a surface-dominant response. To assign the correct process to the observed effect, it is instructive to derive the frequency dependence of CPGE response for diagrams shown in Fig. 4 (B and C).

A higher-order QCPGE response will be of the form  $j_i^{\text{CPGE}}(\omega = 0) = \beta_{ijkl} q_j E_k(\omega) E_l(-\omega)$ , where  $\beta_{ijkl}$  is the fourth-order conductivity tensor,  $q_j$  denotes the first-order dependence of the current on photon momentum, and  $E_k$  and  $E_l$  are the electric field components of the incident light that are down-converted to produce a DC response. We adopt a two-level description for the phenomenon, where one state is an initially filled state below the Fermi energy, while the other is an initially empty state, and the system is driven

by high-energy visible light. Because the material has inversion symmetry, we can assign a definite parity to the states ( $g$  and  $u$ ), with the energy gap between them denoted by  $\Delta$ . These symmetry labels can be interpreted as Wannier representations of two bands in the crystal. In the QCPGE process (Fig. 4B), one vertex couples to the optical field through an electric quadrupole/magnetic dipole, and the other vertex couples through an electric dipole to produce a DC response (two interactions with the field at  $\omega$  and  $-\omega$ ) under no applied bias. In the experimental geometry, light is taken to be incident with a propagation vector along the  $-\hat{z}$  direction ( $b$  axis) (Fig. 1B). We expand the density matrix formalism to second order in the driving fields and extract the part of the current that responds to the circular polarization of the incoming optical field (see section S3 for a detailed derivation). For the QCPGE response, we arrive at an expression for the photocurrent

$$j_\delta(\omega = 0) = -\frac{n}{2} \left( \frac{e^3}{\hbar^2} \right) \frac{[(v_z v_\delta^* + v_z^* v_\delta)(v_\alpha v_\gamma^* - v_\alpha^* v_\gamma)]}{\omega \omega_0^2 (\omega_0^2 - \omega^2)} (q_z E_\alpha(\omega) E_\gamma(-\omega)) \quad (2)$$

This equation gives the value of a current density  $j$  in the direction  $\delta$  driven by circular polarization of light and is first order in  $q_z$ .  $\hbar\omega_0 = \Delta$

is the energy difference between the initially filled and empty states. The terms  $v_z$ ,  $v_\delta$ ,  $v_\alpha$  and  $v_\gamma$  denote velocity matrix elements in the  $\mathcal{H}$ -eigenbasis along the directions denoted by the subscripts. The current density,  $j$ , as given by Eq. 2, is a shift current type response driven by interband coherence expressed in the off-diagonal terms of the density matrix. Calculating the wavelength-dependent CPGE for high-energy excitations produces an antiresonant line shape that is mirrored along the  $j_\delta = 0$  line (Fig. 4D, blue curve). This matches well with the wavelength-dependent CPGE observed experimentally (Fig. 3A). However, an important point to note here is that the expression is odd under  $C_{2z}$  and goes to zero if this symmetry is preserved. Such a response should therefore be absent in a crystal such as the low-temperature phase of  $\text{Ta}_2\text{NiSe}_5$  if it belongs to the group  $C_{2h}$ . This motivates a careful consideration of the symmetries in the low-temperature phase to reconcile with our experimental and theoretical observations.

Before we proceed further, we first inspect the surface term and its possible role in the CPGE response observed in the low-temperature phase of  $\text{Ta}_2\text{NiSe}_5$ . Broken inversion symmetry near the surface would allow an ordinary electric dipole-induced CPGE response. However, because such a current will be exponentially localized to the surface of the system, the outgoing current vertex will involve a transformation  $q_z \mapsto i\kappa$ , where  $\kappa$  is real and positive. To analyze the real part of the current, we also need to make the transformation  $\omega \mapsto \omega + i\eta$ . The output DC response is again generated by an even-parity quadrupole operator and is produced by the second-order ground-state population shift  $\rho_{11}^{(2)}$ . We can write the corresponding nonlinear photocurrent corresponding to this process as

$$j_\delta(\omega = 0) = \frac{\tau}{\omega\Delta} (v_z v_\delta^* + v_z^* v_\delta) (v_\alpha^* v_\beta - v_\alpha v_\beta^*) \left[ \frac{2i\eta}{(\Delta^2 - \omega^2)^2 + 4\omega^2 \eta^2} \right] (q_z E_\alpha(\omega) E_\beta(-\omega)) \quad (3)$$

where the symbols denote previously defined quantities (see section S4 for derivation). Note that, here, we have the substitution  $\frac{1}{\Delta^2} \mapsto \frac{\tau}{\Delta}$  where  $\tau$  is the lifetime of the excited carriers and indicates that the process describes an injection rate and is not a coherently driven process unlike the bulk photocurrent described by Eq. 2. The wavelength-dependent CPGE current for the surface response from Eq. 3 produces a Lorentzian line shape on resonance and does not reverse its sign (Fig. 4D, red curve) and therefore does not match the experimental results (Fig. 3A). We note that there could be a small subdominant contribution from such an effect in the data. In addition, we note that the surface response is also forbidden in the presence of a  $C_{2z}$  symmetry. Thus, broken  $C_{2z}$  symmetry is an unavoidable requirement for any potential CPGE response in  $\text{Ta}_2\text{NiSe}_5$ . A  $C_{2h}$  point group does not allow a CPGE response for light normally incident along the principal axis, and hence, we conclude that the presence of CPGE in the low-temperature phase  $\text{Ta}_2\text{NiSe}_5$  excludes the possibility of a monoclinic point group. Instead, a slightly distorted structure in a triclinic point group breaks  $C_{2z}$  symmetry and activates this response. This distortion can arise naturally from an exchange coupling that hybridizes bands of opposite parity with respect to the  $C_{2z}$ .

To model the Hamiltonian for interacting electrons in  $\text{Ta}_2\text{NiSe}_5$ , we consider intrachain density-density interactions of the form  $V \sum_{\{i \in \text{Ta}\}} \sum_{\{j \in \text{Ni}\}} \hat{n}_i \hat{n}_j$ , where  $V$  describes the strength of the intrachain density-density interactions between Ta and Ni sites and  $\hat{n}_i$  and  $\hat{n}_j$  are the electron densities at the Ta and Ni sites, respectively (25). Here, the spin indices are suppressed, and the sums are over d-orbital-like maximally localized Wannier functions (MLWFs). In a mean-field

decoupling of the interaction term results in  $(c_i^\dagger c_j) (c_j^\dagger c_i) = (c_i^\dagger c_j) \Delta_{ij}$ , where  $c_i$  and  $c_j$  are the annihilation operators at Ta and Ni sites, respectively, and  $\Delta_{ij}$  is taken to be the hybridization-dependent order parameter of the system (25). The order parameter, while being defined using the electronic state of the system, also defines the structural transition and is only nonzero in the low-temperature phase of  $\text{Ta}_2\text{NiSe}_5$ . These set of assumptions lead to the conclusion that the structural symmetry can be broken through hybridization of the low-energy bands, and the details depend on the symmetry of the order parameter, which was further constrained by  $C_{2h}$  point group symmetry.

To perform a more accurate analysis of the many-body state in  $\text{Ta}_2\text{NiSe}_5$ , we start with classifying the MLWFs by their symmetries under  $C_{2h}$ . We note that the states comprising top of the valence band and bottom of the conduction band are made of d-orbitals belonging to the  $B_g$  and  $A_g$  irreducible representations under this assignment. Hence, the interaction terms can be denoted by the diagrams shown in Fig. 4E and have the form  $U_{\text{inter}} \Psi_{A_g}^\dagger \Psi_{A_g} \Psi_{B_g}^\dagger \Psi_{B_g}$ , where  $\Psi_{A_g(B_g)}$  and  $\Psi_{A_g(B_g)}^\dagger$  annihilate and create electrons, respectively, in the state belonging to the irreducible representation  $A_g(B_g)$ . The diagrams contain both direct density-density interactions and exchange interactions, and the interaction energy term can be written in a mean-field form as

$$U_{\text{inter}} [\Psi_{A_g}^\dagger \Psi_{A_g} \langle \Psi_{B_g}^\dagger \Psi_{B_g} \rangle - \Psi_{A_g}^\dagger \Psi_{B_g} \langle \Psi_{B_g}^\dagger \Psi_{A_g} \rangle] \quad (4)$$

The exchange term containing the expectation value  $\langle \Psi_{B_g}^\dagger \Psi_{A_g} \rangle$  that defines an order parameter for the phase transition (25) can be present only if the monoclinic point group  $C_{2h}$  is spontaneously broken to the triclinic point group  $C_i$ , because the exchange term preserves inversion but breaks  $C_{2z}$  and  $\sigma_z$  symmetries. The two orbitals defining the valence and conduction band edges thus cannot hybridize if they belong to irreducible representations with opposite characters for the  $C_{2z}$  or  $\sigma_z$  symmetries, and this hybridization is only possible when these symmetries are spontaneously broken. Therefore, such an order parameter would necessarily allow a nonzero (although possibly small) triclinic distortion in the system, while preserving inversion symmetry. Because this order parameter also considers the  $z$ -dependent symmetries of  $\text{Ta}_2\text{NiSe}_5$  while defining the hybridization, it more accurately represents the structural transition  $\text{Ta}_2\text{NiSe}_5$  than previous analyses, which had considered a more simplified 2D structure of the system. We note that applying a bias comparable to the bandgap of  $\text{Ta}_2\text{NiSe}_5$  (Fig. 3B) injects carriers that occupy the two complementary states exchange split by the mean-field potential effectively setting its value to zero. This effectively restores the  $C_2$  symmetry of the system and nulls the CPGE response. First-principles calculations (25, 29, 44) have also suggested such a slight triclinic distortion in the ground state, providing further support for this scenario. Even a small distortion that breaks  $C_{2z}$  can activate higher-order processes such as QCPGE, thereby rendering it observable.

An interesting picture therefore emerges from the study is that the structure of  $\text{Ta}_2\text{NiSe}_5$  in the low-temperature phase is not a proper monoclinic structure but has a small triclinic distortion. Such a distortion can be associated with an exchange coupling order parameter  $\langle \Psi_{B_g}^\dagger \Psi_{A_g} \rangle$  that spontaneously breaks the  $C_2$  axis along the crystallographic  $b$  axis. The breaking of  $C_2$  symmetry has the important consequence of allowing the QCPGE processes to be nonzero, which are otherwise disallowed in the monoclinic phase. The effect, as shown earlier, cannot be explained using surface effects because of the fact that such a process will have a symmetric line shape and will not

show a sign change when the excitation energy is changed, as we observed. Therefore, the effect is mainly governed by the QCPGE process described by Eq. 2. Furthermore, Eq. 2 gives a linear dependence of the QCPGE response on  $q_z$ . As shown in Fig. 3C, mechanical cleavage of a crystal during exfoliation leads to two new surfaces with opposite arrangements of Ta dipoles in a unit cell (clockwise or anticlockwise around a Ni atom), which makes the two surfaces enantiomeric with respect to each other. Thus, probing the two faces is effectively making the change  $q_z \leftrightarrow -q_z$ , because it is analogous to studying the crystal from the top or bottom. A change of  $q_z \leftrightarrow -q_z$  will lead to a reversal of the current density obtained using Eq. 2, and so, such a change explains the behavior of the two devices with mirrored (opposite) CPGE response (Fig. 3A).

In conclusion, we have developed a new spectroscopic probe, QCPGE, to study a previously elusive symmetry breaking in a potential EI material,  $\text{Ta}_2\text{NiSe}_5$ . Conventional, electric dipole-induced CPGE is disallowed in  $\text{Ta}_2\text{NiSe}_5$  with bulk inversion symmetry. However, a non-zero CPGE can be triggered by higher-order multipolar coupling with the driving field but under a broken  $C_{2z}$  symmetry. The exchange coupling in the system that also defines the order parameter for the phase transition in the system leads to a broken  $C_{2z}$  while preserving inversion symmetry, implying that  $\text{Ta}_2\text{NiSe}_5$  is in a triclinic point group  $C_i$  in the low-temperature phase. Although the distortion can be small to be visualized structurally, it has measurable effects on the electronic properties of the material. We believe that the QCPGE technique can be extended to study the optoelectronic transport behavior of other centrosymmetric materials with broken symmetries or potentially hidden asymmetries that can be difficult to probe otherwise. More generally, our work adds new insights as to how electronic correlations such as hybridizations can have important implications on the crystalline symmetries, and these details must be fully considered when analyzing strongly correlated systems.

## MATERIALS AND METHODS

### Material synthesis

High-quality single crystals of  $\text{Ta}_2\text{NiSe}_5$  were grown by chemical vapor transport method. A finely ground polycrystalline sample of  $\text{Ta}_2\text{NiSe}_5$  prepared as described in (45) was loaded and sealed under vacuum in a quartz ampoule together with small amounts of iodine as the transporting agent. Subsequently, the sealed ampoule was placed in a three-zone tube furnace, under a temperature gradient of 870°C/820°C. After 10 days of growth, needle-shaped single crystals were obtained at the cold part of the ampoule.

X-ray diffraction (powder diffraction, Bruker D8 diffractometer, Cu K $\alpha$  radiation), single-crystal x-ray (Bruker, KAPPA APEX II CCD DUO, Mo K $\alpha$  radiation), Laue diffraction (Photonic Science), and scanning electron microscopes (ZEISS Ultra Plus) equipped with an energy-dispersive x-ray spectroscopy probe were used to determine single-crystal quality, phase purity, crystal structure parameters, morphology, and chemical composition. The experimental characterization of physical properties, such as electrical resistivity, was carried out using a Physical Property Measurement System (Quantum Design, USA). Electrical resistivity and  $ac$  plane x-ray diffraction are shown in figs. S1 and S2, respectively.

### Device fabrication

Large flakes were mechanically exfoliated from the  $\text{Ta}_2\text{NiSe}_5$  single crystals and placed on Si/SiO<sub>2</sub> substrates. Electrodes were patterned

using electron beam lithography, followed by physical vapor deposition of 300-nm Ti and 100-nm Au. All measurements were performed within a week of device fabrication inside a vacuum cryostat to avoid degradation.

### Photocurrent measurements

A supercontinuum laser (NKT Photonics) was used, and wavelengths in the range of 400 to 800 nm were filtered using SuperK VARIA filter. The laser was mechanically chopped using a chopper that was connected to the lock-in amplifier (SRS 830). The laser was focused on the sample using a 60 $\times$  objective lens in a home-built setup to achieve a spot size of 2- $\mu\text{m}$  full width at half maximum. The laser power on the device was maintained at 0.25 mW unless otherwise specified. The polarization of the laser was fixed along the  $a$  axis of the crystal (identified visually as the long axis of the flake), and the helicity of light was precisely controlled using a QWP through a motorized rotation holder with servo motor drive (Thorlabs). The output current from the devices was recorded continuously ( $\sim 10$  data points/s) by the Peripheral Component Interconnect (PCI) card (National Instruments, NI PCI-6281). Measurements were repeated several times on each device to ensure repeatability. For high-temperature measurements, a Peltier heated stage with a temperature controller (TE Technology) was used to precisely control the temperature of the sample. Keithley 2635B source measure unit (SMU) was used to apply DC bias to the samples.

### SUPPLEMENTARY MATERIALS

Supplementary material for this article is available at <https://science.org/doi/10.1126/sciadv.abl9020>

### REFERENCES AND NOTES

1. C. Kittel, Physical theory of ferromagnetic domains. *Rev. Mod. Phys.* **21**, 541–583 (1949).
2. P. Toledano, J. Toledano, *Landau Theory Of Phase Transitions, The: Application To Structural, Incommensurate, Magnetic And Liquid Crystal Systems* (World Scientific Publishing Company, ed. 3, 1987).
3. N. Read, S. Sachdev, J. Ye, Landau theory of quantum spin glasses of rotors and Ising spins. *Phys. Rev. B* **52**, 384–410 (1995).
4. B. Rosenstein, D. Li, Ginzburg-Landau theory of type II superconductors in magnetic field. *Rev. Mod. Phys.* **82**, 109–168 (2010).
5. S. Artyukhin, K. T. Delaney, N. A. Spaldin, M. Mostovoy, Landau theory of topological defects in multiferroic hexagonal manganites. *Nat. Mater.* **13**, 42–49 (2014).
6. W. Kohn, J. M. Luttinger, New mechanism for superconductivity. *Phys. Rev. Lett.* **15**, 524–526 (1965).
7. M. Fabrizio, A. O. Gogolin, A. A. Nersisyan, From band insulator to Mott insulator in one dimension. *Phys. Rev. Lett.* **83**, 2014–2017 (1999).
8. Y. Zhou, K. Kanoda, T. K. Ng, Quantum spin liquid states. *Rev. Mod. Phys.* **89**, 025003 (2017).
9. H. V. Löhneysen, A. Rosch, M. Vojta, P. Wölfle, Fermi-liquid instabilities at magnetic quantum phase transitions. *Rev. Mod. Phys.* **79**, 1015–1075 (2007).
10. D. Reznik, L. Pintschovius, M. Ito, S. Iikubo, M. Sato, H. Goka, M. Fujita, K. Yamada, G. D. Gu, J. M. Tranquada, Electron-phonon coupling reflecting dynamic charge inhomogeneity in copper oxide superconductors. *Nature* **440**, 1170–1173 (2006).
11. K. S. Burch, S. V. Dordevic, F. P. Mena, A. B. Kuzmenko, D. Van Der Marel, J. L. Sarrao, J. R. Jeffries, E. D. Bauer, M. B. Maple, D. N. Basov, Optical signatures of momentum-dependent hybridization of the local moments and conduction electrons in Kondo lattices. *Phys. Rev. B* **75**, 054523 (2007).
12. D. Jérôme, T. M. Rice, W. Kohn, Excitonic insulator. *Phys. Rev.* **158**, 462–475 (1967).
13. P. Bucher, P. Steiner, P. Wachter, Excitonic insulator phase in  $\text{TmSe}_{0.45}\text{Te}_{0.55}$ . *Phys. Rev. Lett.* **67**, 2717–2720 (1991).
14. P. Wachter, The discovery of excitonium. *J. Alloys Compd.* **225**, 133–138 (1995).
15. F. X. Bronold, H. Fehske, Possibility of an excitonic insulator at the semiconductor-semimetal transition. *Phys. Rev. B* **74**, 165107 (2006).
16. P. Wachter, Exciton condensation in an intermediate valence compound:  $\text{TmSe}_{0.45}\text{Te}_{0.55}$ . *Solid State Commun.* **118**, 645–650 (2001).
17. S. Koley, M. S. Laad, N. S. Vidhyadhiraja, A. Taraphder, Preformed excitons, orbital selectivity, and charge density wave order in  $1\text{T-TiSe}_2$ . *Phys. Rev. B* **90**, 115146 (2014).

18. H. Cercellier, C. Monney, F. Clerc, C. Battaglia, L. Despont, M. G. Garnier, H. Beck, P. Aebi, L. Patthey, H. Berger, L. Forró, Evidence for an excitonic insulator phase in 1T-TiSe<sub>2</sub>. *Phys. Rev. Lett.* **99**, 146403 (2007).
19. Y. Wakasaka, T. Sudayama, K. Takubo, T. Mizokawa, M. Arita, H. Namatame, M. Taniguchi, N. Katayama, M. Nohara, H. Takagi, Excitonic insulator state in Ta<sub>2</sub>NiSe<sub>5</sub> probed by photoemission spectroscopy. *Phys. Rev. Lett.* **103**, 026402 (2009).
20. T. Kaneko, T. Toriyama, T. Konishi, Y. Ohta, Orthorhombic-to-monoclinic phase transition of Ta<sub>2</sub>NiSe<sub>5</sub> induced by the Bose-Einstein condensation of excitons. *Phys. Rev. B* **87**, 035121 (2013).
21. P. Wächter, B. Bucher, Exciton condensation and its influence on the specific heat. *Phys. B Condens. Matter.* **408**, 51–57 (2013).
22. J. Ishioka, Y. H. Liu, K. Shimatake, T. Kurosawa, K. Ichimura, Y. Toda, M. Oda, S. Tanda, Chiral charge-density waves. *Phys. Rev. Lett.* **105**, 176401 (2010).
23. A. Nakano, T. Hasegawa, S. Tamura, N. Katayama, S. Tsutsui, H. Sawa, Antiferroelectric distortion with anomalous phonon softening in the excitonic insulator Ta<sub>2</sub>NiSe<sub>5</sub>. *Phys. Rev. B* **98**, 045139 (2018).
24. K. Fukutani, R. Stania, C. Il Kwon, J. S. Kim, K. J. Kong, J. Kim, H. W. Yeom, Detecting photoelectrons from spontaneously formed excitons. *Nat. Phys.* **17**, 1024–1030 (2021).
25. G. Mazza, M. Rösner, L. Windgätter, S. Latini, H. Hübener, A. J. Millis, A. Rubio, A. Georges, Nature of symmetry breaking at the excitonic insulator transition: Ta<sub>2</sub>NiSe<sub>5</sub>. *Phys. Rev. Lett.* **124**, 197601 (2020).
26. M. D. Watson, I. Marković, E. A. Morales, P. Le Fèvre, M. Merz, A. A. Haghighirad, P. D. C. King, Band hybridization at the semimetal-semiconductor transition of Ta<sub>2</sub>NiSe<sub>5</sub> enabled by mirror-symmetry breaking. *Phys. Rev. Res.* **2**, 013236 (2020).
27. H. M. Bretscher, P. Andrich, P. Telang, A. Singh, L. Harnagea, A. K. Sood, A. Rao, Ultrafast melting and recovery of collective order in the excitonic insulator Ta<sub>2</sub>NiSe<sub>5</sub>. *Nat. Commun.* **12**, 1699 (2021).
28. H. M. Bretscher, P. Andrich, Y. Murakami, D. Golež, B. Remez, P. Telang, A. Singh, L. Harnagea, N. R. Cooper, A. J. Millis, P. Werner, A. K. Sood, A. Rao, Imaging the coherent propagation of collective modes in the excitonic insulator candidate Ta<sub>2</sub>NiSe<sub>5</sub> at room temperature. *Sci. Adv.* **7**, eabd6147 (2021).
29. E. Baldini, A. Zong, D. Choi, C. Lee, M. H. Michael, L. Windgätter, I. I. Mazin, S. Latini, D. Azoury, B. Lv, A. Kogar, Y. Wang, Y. Lu, T. Takayama, H. Takagi, A. J. Millis, A. Rubio, E. Demler, N. Gedik, The spontaneous symmetry breaking in Ta<sub>2</sub>NiSe<sub>5</sub> is structural in nature. arXiv:2007.02909 [cond-mat.str-el] (6 July 2020).
30. E. L. Ivchenko, *Optical Spectroscopy of Semiconductor Nanostructures* (Alpha Science Int'l Ltd., 2005).
31. S. Dhara, E. J. Mele, R. Agarwal, Voltage-tunable circular photogalvanic effect in silicon nanowires. *Science* **349**, 726–729 (2015).
32. Z. Ji, G. Liu, Z. Addison, W. Liu, P. Yu, H. Gao, Z. Liu, A. M. Rappe, C. L. Kane, E. J. Mele, R. Agarwal, Spatially dispersive circular photogalvanic effect in a Weyl semimetal. *Nat. Mater.* **18**, 955–962 (2019).
33. H. Plank, S. A. Tarasenko, T. Hummel, G. Knebl, P. Pfeffer, M. Kamp, S. Höfling, S. D. Ganichev, Circular and linear photogalvanic effects in type-II GaSb/InAs quantum well structures in the inverted regime. *Phys. E Low Dimensional Syst. Nanostruct.* **85**, 193–198 (2017).
34. S. W. Cheong, SOS: Symmetry-operational similarity. *npj Quantum Mater.* **4**, 53 (2019).
35. B. T. Fichera, A. Kogar, L. Ye, B. Gökçe, A. Zong, J. G. Checkelsky, N. Gedik, Second harmonic generation as a probe of broken mirror symmetry. *Phys. Rev. B* **101**, 241106 (2020).
36. F. De Juan, A. G. Grushin, T. Morimoto, J. E. Moore, Quantized circular photogalvanic effect in Weyl semimetals. *Nat. Commun.* **8**, 15995 (2017).
37. Z. Ji, W. Liu, S. Krylyuk, X. Fan, Z. Zhang, A. Pan, L. Feng, A. Davydov, R. Agarwal, Photocurrent detection of the orbital angular momentum of light. *Science* **368**, 763–767 (2020).
38. P. Hosur, Circular photogalvanic effect on topological insulator surfaces: Berry-curvature-dependent response. *Phys. Rev. B* **83**, 035309 (2011).
39. J. Quereda, T. S. Ghiasi, J. S. You, J. van den Brink, B. J. van Wees, C. H. van der Wal, Symmetry regimes for circular photocurrents in monolayer MoSe<sub>2</sub>. *Nat. Commun.* **9**, 3346 (2018).
40. F. J. Di Salvo, C. H. Chen, R. M. Fleming, J. V. Waszczak, R. G. Dunn, S. A. Sunshine, J. A. Ibers, Physical and structural properties of the new layered compounds Ta<sub>2</sub>Ni<sub>5</sub> and Ta<sub>2</sub>NiSe<sub>5</sub>. *J. Less Common Met.* **116**, 51–61 (1986).
41. M. Ye, P. A. Volkov, H. Lohani, I. Feldman, M. Kim, A. Kanigel, G. Blumberg, Lattice dynamics of the excitonic insulator Ta<sub>2</sub>Ni(Se<sub>1-x</sub>S<sub>x</sub>)<sub>5</sub>. *Phys. Rev. B* **104**, 045102 (2021).
42. A. Rasmita, C. Jiang, H. Ma, Z. Ji, R. Agarwal, W. Gao, Tunable geometric photocurrent in van der Waals heterostructure. *Optica* **7**, 1204 (2020).
43. Y. F. Lu, H. Kono, T. I. Larkin, A. W. Rost, T. Takayama, A. V. Boris, B. Keimer, H. Takagi, Zero-gap semiconductor to excitonic insulator transition in Ta<sub>2</sub>NiSe<sub>5</sub>. *Nat. Commun.* **8**, 14408 (2017).
44. L. Windgätter, M. Rösner, G. Mazza, H. Hübener, A. Georges, A. J. Millis, S. Latini, A. Rubio, Common microscopic origin of the phase transitions in Ta<sub>2</sub>Ni<sub>5</sub> and the excitonic insulator candidate Ta<sub>2</sub>NiSe<sub>5</sub>. arXiv:2105.13924 [cond-mat.mtrl-sci] (5 June 2021).
45. S. Pal, S. Grover, L. Harnagea, P. Telang, A. Singh, D. V. S. Muthu, U. V. Waghmare, A. K. Sood, Destabilizing excitonic insulator phase by pressure tuning of exciton-phonon coupling. *Phys. Rev. Res.* **2**, 043182 (2020).

#### Acknowledgments

**Funding:** This work was supported by the U.S. Army Research Office (grant no. W911NF-17-1-0436) and the U.S. Air Force Office of Scientific Research (award no. FA9550-20-1-0345). L.H. acknowledges the financial support from the Department of Science and Technology (DST), India [grant no. SR/WOS-A/PM-33/ 2018 (G)] and IISER Pune for providing the facilities for crystal growth/characterization. **Author contributions:** H.J. and R.A. conceptualized the project. L.H. synthesized the required materials. H.J., E.J.M., and R.A. formulated the experiments and performed theoretical investigation. H.J. fabricated the devices and performed all optoelectronic experiments. E.J.M. and R.A. acquired funding for the project. H.J. and R.A. drafted the paper, and all authors contributed to reviewing and editing the final draft. R.A. supervised the project. **Competing interests:** The authors declare that they have no competing interests. **Data and materials availability:** All data needed to evaluate the conclusions in the paper are present in the paper and/or the Supplementary Materials.

Submitted 12 August 2021

Accepted 22 December 2021

Published 16 February 2022

10.1126/sciadv.abl9020